

IS THERE A BLACK HOLE IN NGC 4382?*

KAYHAN GÜLTEKIN¹, DOUGLAS O. RICHSTONE¹, KARL GEBHARDT², S. M. FABER³, TOD R. LAUER⁴, RALF BENDER⁵,
JOHN KORMENDY², AND JASON PINKNEY⁶

¹ Department of Astronomy, University of Michigan, Ann Arbor, MI 48109, USA; kayhan@umich.edu

² Department of Astronomy, University of Texas, Austin, TX 78712, USA

³ University of California Observatories/Lick Observatory, Board of Studies in Astronomy and Astrophysics,
University of California, Santa Cruz, CA 95064, USA

⁴ National Optical Astronomy Observatory, Tucson, AZ 85726, USA

⁵ Universitäts-Sternwarte München, Ludwig-Maximilians-Universität, Scheinerstr. 1, D-81679, Germany

⁶ Department of Physics and Astronomy, Ohio Northern University, Ada, OH 45810, USA

Received 2010 November 30; accepted 2011 August 1; published 2011 October 13

ABSTRACT

We present *Hubble Space Telescope* (*HST*) Space Telescope Imaging Spectrograph observations of the galaxy NGC 4382 (M85) and axisymmetric models of the galaxy to determine mass-to-light ratio (Υ_V) and central black hole mass (M_{BH}). We find $\Upsilon_V = 3.74 \pm 0.1 M_\odot/L_\odot$ and $M_{\text{BH}} = 1.3^{+5.2}_{-1.2} \times 10^7 M_\odot$ at an assumed distance of 17.9 Mpc, consistent with no black hole. The upper limit, $M_{\text{BH}} < 9.6 \times 10^7 M_\odot (2\sigma)$ or $M_{\text{BH}} < 1.4 \times 10^8 (3\sigma)$, is consistent with the current $M-\sigma$ relation, which predicts $M_{\text{BH}} = 8.8 \times 10^7 M_\odot$ at $\sigma_e = 182 \text{ km s}^{-1}$, but low for the current $M-L$ relation, which predicts $M_{\text{BH}} = 7.8 \times 10^8 M_\odot$ at $L_V = 8.9 \times 10^{10} L_{\odot,V}$. *HST* images show the nucleus to be double, suggesting the presence of a nuclear eccentric stellar disk, analogous to the Tremaine disk in M31. This conclusion is supported by the *HST* velocity dispersion profile. Despite the presence of this non-axisymmetric feature and evidence of a recent merger, we conclude that the reliability of our black hole mass determination is not hindered. The inferred low black hole mass may explain the lack of nuclear activity.

Key words: black hole physics – galaxies: individual (NGC 4382, M85) – galaxies: kinematics and dynamics – galaxies: nuclei

Online-only material: color figures

1. INTRODUCTION

Finding a black hole at the center of a galaxy is no longer a surprise. The prevalence of these black holes is well established (Richstone et al. 1998). Their importance has also been recognized, for example, as active galactic nuclei (AGNs) central engines (Rees 1984). The tight correlation of black hole masses with host galaxy properties strongly suggests an underlying link between galaxy and black hole evolution. The black hole mass has been found to be correlated with the stellar spheroid’s mass (Dressler 1989; Magorrian et al. 1998; Laor 2001; McLure & Dunlop 2002; Marconi & Hunt 2003; Häring & Rix 2004), luminosity (the $M-L$ relation, Kormendy 1993; Kormendy & Richstone 1995; Magorrian et al. 1998; Kormendy & Gebhardt 2001; Gültekin et al. 2009c), stellar velocity dispersion (the $M-\sigma$ relation, Ferrarese & Merritt 2000; Gebhardt et al. 2000; Tremaine et al. 2002; Gültekin et al. 2009c), galaxy core parameters (Milosavljević et al. 2002; Ravindranath et al. 2002; Graham 2004; Ferrarese et al. 2006; Merritt 2006; Lauer et al. 2007b; Kormendy & Bender 2009), and globular cluster system (Burkert & Tremaine 2010). Current theoretical work addressing these scaling relations focuses on feedback from outflows that are powered by accretion onto the central black hole. Thus, the consequences of black hole growth play a role in regulating star formation in the galaxy (e.g., Bower et al. 2006; Hopkins et al. 2006). Despite this progress, we do not have a complete

understanding of the physics involved, and the pursuit of black hole masses remains important.

Masses found from primary, direct, dynamical measurements are the basis from which all other black hole masses are derived. Indirect mass indicators, such as AGN line widths, are calibrated to reverberation mapping, direct yet secondary measurements (Bentz et al. 2006), which are themselves normalized against the direct dynamical measurements (Onken et al. 2004; Woo et al. 2010). Currently, even the empirical scaling relations are incomplete. The $M-L$ and $M-\sigma$ relations make different predictions at the upper end (Lauer et al. 2007a). The possibility of increased intrinsic scatter at the low end remains untested (Volonteri 2007), and there is growing evidence that late-type galaxies as a whole and pseudo-bulges in particular do not lie on the same relation as early-type galaxies (Hu 2008; Gültekin et al. 2009c; Greene et al. 2010; Kormendy et al. 2010). There is also much interest in multi-parameter extensions to these relations (Aller & Richstone 2007; Hopkins et al. 2007).

It is this last open question, the existence and utility of multi-parameter scaling relations, for which the galaxy in this study, NGC 4382 (M85), was selected. NGC 4382 lies in a narrow range in velocity dispersion ($180 \text{ km s}^{-1} < \sigma < 220 \text{ km s}^{-1}$, for which $M_{\text{BH}} \sim 10^8 M_\odot$) based on HyperLEDA⁷ central velocity dispersion measures (Paturel et al. 2003). With enough galaxies from a narrow range in velocity dispersion, we may test for additional trends in black hole mass with other host galaxy parameters. This range was chosen because galaxies in this range may have either core or power-law surface brightness profiles and because both late-type and early-type galaxies lie in this range. The galaxies were also selected based on their

* Based on observations made with the *Hubble Space Telescope*, obtained at the Space Telescope Science Institute, which is operated by the Association of Universities for Research in Astronomy, Inc., under NASA contract NAS 5-26555. These observations are associated with GO proposals 5999, 6587, 6633, 7468, and 9107.

⁷ Available at <http://leda.univ-lyon1.fr/>.

distances so that the predicted radius of influence was larger than $0''.1$. The radius of influence is defined as

$$R_{\text{infl}} \equiv \frac{GM_{\text{BH}}}{\sigma^2(R_{\text{infl}})}, \quad (1)$$

where the velocity dispersion $\sigma(R)$ is a function of projected distance from the center along the major axis and is evaluated at the radius of influence. Black hole masses were estimated from their central velocity dispersion measurement and the M – σ fit due to Tremaine et al. (2002).

NGC 4382 is an E2 galaxy (Kormendy et al. 2009) with diffuse stellar light surrounding it, which has led some to classify it as an S0 (de Vaucouleurs et al. 1991). We take the distance to NGC 4382 to be 17.9 Mpc (calculated assuming a Hubble constant of $H_0 = 70 \text{ km s}^{-1} \text{ Mpc}^{-1}$). The surface brightness profile as a function of radius reveals a core at the center (Lauer et al. 2005) and may be parameterized with a ‘‘Nuker law’’ given by

$$I(r) = 2^{(\beta-\gamma)/\alpha} I_b \left(\frac{r_b}{r}\right)^\gamma \left[1 + \left(\frac{r}{r_b}\right)^\alpha\right]^{(\gamma-\beta)/\alpha}, \quad (2)$$

which is a broken power-law profile with variable sharpness in the break (Lauer et al. 1995). NGC 4382 has $r_b = 0''.93 = 80.7 \text{ pc}$, $I_b = 15.67 \text{ mag arcsec}^{-2}$, $\alpha = 1.13$, $\beta = 1.39$, and $\gamma = 0.00$ (Lauer et al. 2005). The total luminosity of the galaxy is $M_V = -22.54$.

In Section 2 we describe the observations and data reduction, including new space spectroscopic observations (Section 2.1), ground-based spectra (Section 2.2), and imaging data (Section 2.3). The kinematic modeling and its results are presented in Section 3, and we discuss the caveats for and implications of our results in Section 4.

2. OBSERVATIONS

2.1. STIS Observations and Data Reduction

Measuring black hole masses precisely requires spectra with high spatial resolution. Thus, most precise black hole mass measurements come from observations using the *Hubble Space Telescope* (*HST*), though adaptive optics techniques are showing promise (e.g., Krajnóvić et al. 2009; Nowak et al. 2010; Gebhardt et al. 2011) and mass measurements using maser observations are ramping up (Kuo et al. 2010). We observed Ca II triplet absorption from NGC 4382 with the Space Telescope Imaging Spectrograph (STIS) on *HST* set with the G750M grating and a $52'' \times 0''.2$ slit. The medium-dispersion grating, as opposed to the low-dispersion G750L grating, is necessary in order to get the spectral resolution high enough to recover line-of-sight velocity distributions (LOSVDs) with sufficient precision. The slit was set at a width of $0''.2$ to optimize the signal-to-noise ratio as core ellipticals have relatively low central surface brightness and widening the slit as far as possible allows as short an observation as possible. The slit was positioned along a position angle of P.A. = 48° east of north close to the photometric major axis position angle of P.A. = 30° as determined from *HST*/Wide Field Planetary Camera 2 (WFPC2) observations (see Section 2.3 below; Lauer et al. 2005; Kormendy et al. 2009). We obtained 16 exposures at five dither positions for a total of exposure of 18,794 s. The STIS CCD has a 1024×1024 pixel format, a readout noise of $\sim 1e^-$ pixel $^{-1}$, and a gain of 1.0 without on-chip binning. The spectra spanned a wavelength range of 8257–8847 Å, and our wavelength solutions revealed a reciprocal dispersion of

Table 1
Kinematic Profile for NGC 4382 from STIS Observations

R ('')	Width (pixel)	V (km s $^{-1}$)	σ (km s $^{-1}$)	h_3	h_4
0.00	1	15 ± 17	147 ± 20	-0.017 ± 0.06	-0.068 ± 0.060
0.05	1	4 ± 14	162 ± 12	-0.049 ± 0.05	-0.045 ± 0.036
0.10	1	24 ± 15	150 ± 13	-0.006 ± 0.05	-0.067 ± 0.029
0.18	2	31 ± 15	145 ± 12	-0.071 ± 0.05	-0.049 ± 0.032
0.30	3	14 ± 16	170 ± 17	0.021 ± 0.06	-0.063 ± 0.046
0.58	8	24 ± 18	178 ± 20	-0.021 ± 0.07	-0.016 ± 0.053
1.12	14	20 ± 19	166 ± 20	-0.001 ± 0.07	0.015 ± 0.060

Notes. Gauss–Hermite moments for velocity profiles derived from STIS data. First and second moments are given in units of km s $^{-1}$. Radii are given in arcsec and the second column gives the width of the radial bin in pixels, which are $0''.051$.

$0.554 \text{ \AA pixel}^{-1}$, and the spatial scale was $0''.05071 \text{ pixel}^{-1}$ for G750M at 8561 Å.

The STIS data reduction was done with routines developed for this purpose (Pence 1998; Pinkney et al. 2003) following the standard pipeline: raw spectra were extracted from the multi-dimensional FITS file, and then a constant fit to the overscan region was subtracted to remove the bias level. The STIS CCD has warm and hot pixels that change on timescales of about a day. These pixels require that the subtraction of dark current be accurate, which we accomplished by using the iterative *self-dark* technique (Pinkney et al. 2003). After flat fielding and dark subtraction, spectra were shifted vertically to a common dither, combined, and rotated. One-dimensional spectra were then extracted using a bi-weight combination of rows. Near the galaxy center, we adopted a 1 pixel wide binning for maximum spatial resolution. These data-reduction methods are similar to those in Pinkney et al. (2003), which the interested reader may consult for details.

LOSVDs were extracted from reduced spectra as described in Gültekin et al. (2009b). Each galaxy spectrum is a convolution of the intrinsic spectrum of stars observed in the aperture with the LOSVD of those stars. We deconvolved the observed galaxy spectrum using the template spectrum composed from standard stellar spectra using a maximum penalized-likelihood method (Gebhardt et al. 2003; Pinkney et al. 2003). We present Gauss–Hermite moments of the extracted velocity profiles in Table 1 and Figure 1. Although it is common practice to communicate velocity profiles with Gauss–Hermite moments, we use LOSVDs binned in velocity space for our modeling described below in Section 3.

2.2. Ground-based Spectra

Ground-based velocity information was obtained from archival data using the Spectrographic Areal Unit for Research on Optical Nebulae (SAURON),⁸ an integral-field spectrograph unit mounted on the William Herschel Telescope in La Palma (Bacon et al. 2001). As the SAURON instrument and observations were designed to measure and characterize the internal kinematics of the selected galaxies (de Zeeuw et al. 2002), the data are excellent for our purposes. In its low-resolution mode, the instrument has a field of view of $33 \times 41''$ with $0''.94$ pixels, each of which provides a spectrum with $\text{FWHM} = 4.2 \text{ \AA}$ spectral resolution. This spectral resolution corresponds to $\sigma_{\text{instr}} = 108 \text{ km s}^{-1}$ at 4950 Å, near the center

⁸ Downloaded from <http://www.strw.leidenuniv.nl/sauron/> in 2010 February.

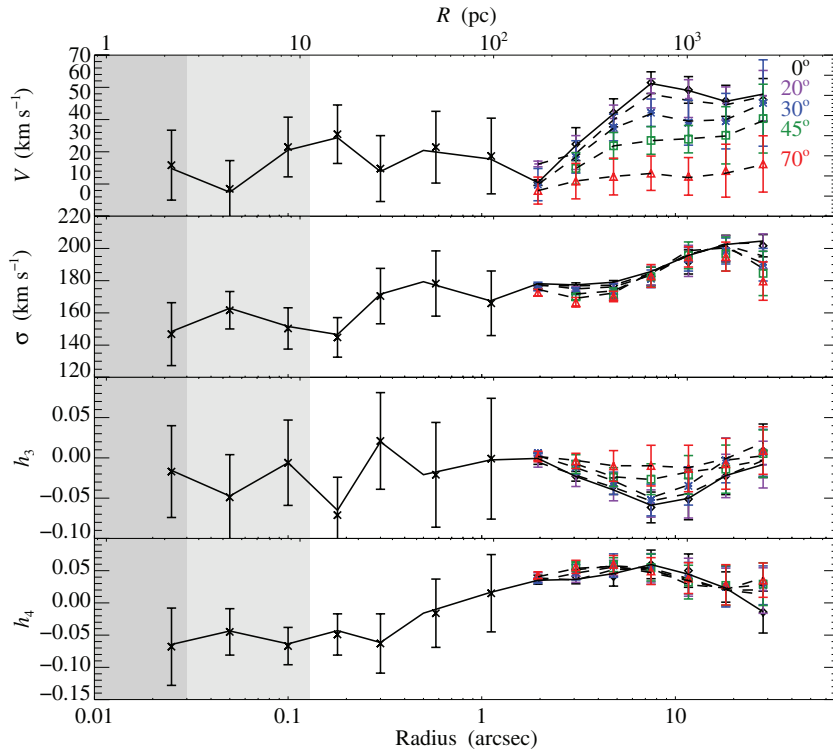


Figure 1. Gauss–Hermite moments of LOSVDs for NGC 4382 as a function of radius, from top to bottom: V , σ , h_3 , and h_4 . Values at the center of the galaxy ($R = 0$) are plotted at $R = 0''.25$. Moments from opposite sides of the galaxy are symmetrized and combined. The sense of the sign is such that radius is increasing to the southwest. Crosses are Gauss–Hermite moments of LOSVDs from *HST* STIS data along the major axis. Also plotted are ground-based Gauss–Hermite moments of LOSVDs along the major axis (black diamonds) and skew axes (other colors with P.A. relative to the major axis indicated on the right in the top panel) from SAURON archives. Though Gauss–Hermite moments are not fit directly in the modeling, the jagged lines are the resulting Gauss–Hermite fit to the best-fit model’s LOSVDs from Section 3 for the major axis (solid) and skew axes (dashed). The best-fit model has $M_{\text{BH}} = 1.5 \times 10^7 M_{\odot}$ and $\Upsilon_V = 3.72$. We indicate the radius of the sphere of influence of a black hole with mass predicted by the M – σ relation (light gray) or with our best-fit mass (medium gray).

(A color version of this figure is available in the online journal.)

of the 4800–5380 Å wavelength range. The data were taken on 2001 March 14 in two pointings, each consisting of four exposures of 1800 s each under $\text{FWHM} = 2''.7$ seeing (Emsellem et al. 2004).

The stellar kinematics data are provided as Gauss–Hermite moments for each lenslet position on the galaxy. The Gauss–Hermite moments from each lenslet were converted into LOSVDs. The data from each quadrant of the galaxy were combined into one, changing signs of the odd moments as necessary. We binned the data into four position angles (0° , 20° , 30° , and 70° east of the major axis) with seven radial bins and one position angle (45° east of the major axis) with six radial bins for a total of 34 LOSVDs from ground-based data.

To incorporate errors in the Gauss–Hermite moments in our data set we created 10^4 Monte Carlo realizations of LOSVDs for each SAURON lenslet. As described in Gültekin et al. (2009b), Gauss–Hermite moments corresponding to unphysical negative values are assigned a value of zero with a conservative uncertainty. For each spatial bin, we took the median LOSVD of all realizations at a given velocity and the standard deviation as the error, which dominated the individual measurement errors. The Gauss–Hermite moments of the LOSVDs are presented in Figure 1 as a function of radius along with our STIS data. These measurements agree well with the ground-based kinematics from Fisher (1997).

The profiles were binned into 13 equal bins in velocity from -500 to 500 km s^{-1} about the systemic velocity covering the range of velocities measured. Using the ground kinematic data,

we compute an effective stellar velocity dispersion, defined as

$$\sigma_e^2 \equiv \frac{\int_0^{R_e} (\sigma(r)^2 + V(r)^2) I(r) dr}{\int_0^{R_e} I(r) dr}, \quad (3)$$

where R_e is the effective radius, $I(r)$ is the surface brightness profile (see Section 2.3 below), and $V(r)$ and $\sigma(r)$ are the first and second Gauss–Hermite moments of the LOSVD. Using a non-parametric method of integrating the brightness and ellipticity profile, Kormendy et al. (2009) find $R_e = 102 \pm 6''$. From the ground-based velocity profile, we find an effective stellar velocity dispersion of $\sigma_e = 182 \pm 5 \text{ km s}^{-1}$.

2.3. Imaging

The high-resolution photometry of the central regions of NGC 4382 comes from WFPC2 observations on *HST* using filters F555W (V) and F814W (I). The observations, data reduction, and surface brightness profiles (including Nuker profile fits) are detailed by Lauer et al. (2005). Surface brightness profiles are also available at the Nuker web page.⁹ The wide-field data that we use are literature data from ground observations on the 1.2 m telescope of the Observatoire de Haute-Provence with point-spread function (PSF) $\text{FWHM} = 3''.12$ originally obtained by Michard & Marchal (1994). The ground data are B -band data, which we have color-corrected with $B - V = 0.9$, determined

⁹ See http://www.noao.edu/noao/staff/lauer/wfpc2_profs/.

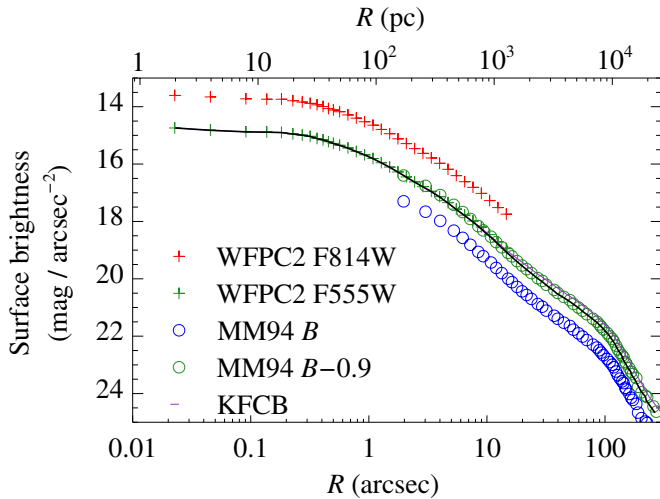


Figure 2. Surface brightness of NGC 4382. Red and green crosses (upper and lower) show F814W and F555W WFPC2 data, respectively, from Lauer et al. (2005). Blue circles show Michard & Marchal (1994) ground photometry from the 1.2 m telescope of the Observatoire de Haute-Provence with a PSF FWHM of $3''.12$. Green circles are the same data but color-shifted by 0.9 mag to match the F555W data. The solid curve is our assumed V-band surface brightness profile of NGC 4382. The purple line is data from Kormendy et al. (2009) and comes from a variety of instruments and bands. The difference between our adopted surface brightness profile and the purple line is small and can be attributed primarily to slightly different colors at large radii.

(A color version of this figure is available in the online journal.)

by requiring the space data and ground data to match where they overlap in the spatial direction. Figure 2 shows the surface brightness profiles of the space and ground data along with our adopted, combined surface brightness profile for our modeling.

Since our modeling efforts began, a superior ground-based photometric data set became available (Kormendy et al. 2009). The data come from several different instruments. Inside of $1''$, it is the same WFPC2 F555W data that we use. Starting at $1''$, the profile is an average of WFPC2 and Advanced Camera for Surveys data as well as two different cameras on the Canada–France–Hawaii Telescope. At the largest radii, the data come from the McDonald 0.8 m telescope, which has a wide field of view. We plot it in Figure 2 for comparison. The agreement inside of $R < 15''$ is striking. At large radii, there is a small but systematic deviation from our adopted surface brightness profile. This is almost certainly due to the different colors used and is likely evidence of a slight color gradient starting outside of $R > 100''$. At these large radii, the smaller PSF of the Kormendy et al. (2009) data set does not have a large advantage, and the extremely wide coverage—out to $R = 625''$ —is not used since our kinematic profiles only go out to $R = 30''$.

3. KINEMATIC MODELING

We use the three-integral, axisymmetric Schwarzschild method to make kinematic models of NGC 4382. The model is constructed in several steps. First the observed surface brightness profile, $\Sigma(r)$, is deprojected into an axisymmetric luminosity density, $j(r, \theta)$. This deprojection assumes that surfaces of constant luminosity density are coaxial ellipsoids and depends on a chosen inclination, which we take to be $i = 90^\circ$. Under the assumption of constant mass-to-light ratio of a chosen value, Υ , the mass density of stars is trivially obtained $\rho(r, \theta) = \Upsilon j$. We can then calculate the stellar gravitational potential from

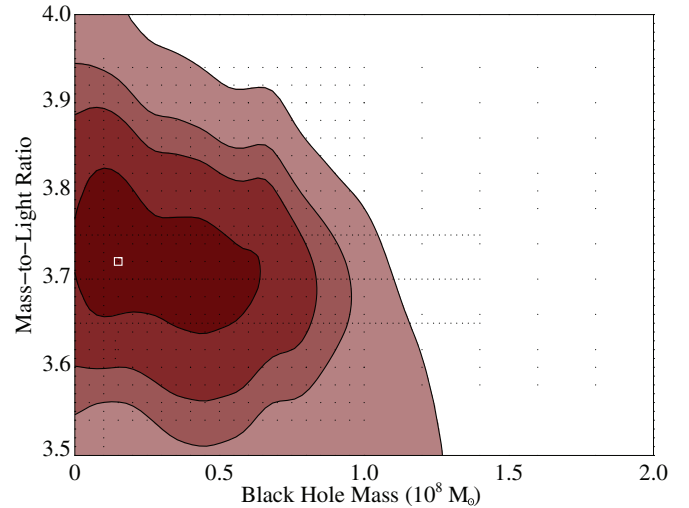


Figure 3. Mass modeling χ^2 contours for NGC 4382. Contours are for $\Delta\chi^2 = 1.00, 2.71, 4.00,$ and 6.63 , which bracket individual parameter confidence levels of 68.3%, 90.0%, 95.4%, and 99.0%, respectively. Contours have been smoothed for plotting, and each level is filled with a solid color. The square shows the best-fit model. Dots indicate parameters modeled. The best-fit model has $M_{\text{BH}} = 1.5 \times 10^7 M_\odot$ and $\Upsilon_V = 3.72 M_\odot/L_{\odot,V}$. Marginalizing over the other parameter we find $M_{\text{BH}} = 1.3^{+5.2}_{-1.2} \times 10^7 M_\odot$ and $\Upsilon_V = 3.74 \pm 0.10 M_\odot/L_{\odot,V}$. (A color version of this figure is available in the online journal.)

Poisson’s equation. The potential from a point mass with a chosen mass, M_{BH} , is then added at $r = 0$.

With the potential for the entire system in hand, we then calculate orbits of representative stars. The number of orbits is different for each mass model with more orbits needed to sample the phase space when either Υ or M_{BH} is large, but the number ranged from 15,735 to 17,213 orbits. The number of orbits is increased by increasing the density of orbits in energy, angular momentum, and non-classical third integral space. We increase the number of orbits with sparsely gridded parameter space (M_{BH} and Υ_V) until our results converge, and then we run a finer grid in parameter space, which we report here. The amount of time each representative star spends in a given bin in position and velocity space is monitored so as to identify the orbits’ possible contribution to the observed surface brightness and LOSVD. For each set of parameters, we find the non-negative weights and a goodness of fit (χ^2) for the set of orbits that best matches the observed LOSVD while reproducing the observed surface brightness. The entire method is explained in more detail in Gebhardt et al. (2003) and Siopis et al. (2009).

To determine what values of M_{BH} and Υ_V to consider, we ran a sparse grid of a wide range of values and then refined around the best-fitting initial guesses. The final ranges considered were $\Upsilon_V = 3.5\text{--}4.0 M_\odot/L_{\odot,V}$ and $M_{\text{BH}} = (0\text{--}2) \times 10^8 M_\odot$. The sampling of parameters was not uniform but may be ascertained from the dots in Figure 3. This figure also plots contours of χ^2 in the $M_{\text{BH}}\text{--}\Upsilon_V$ plane. The best-fit model has parameters $M_{\text{BH}} = 1.5 \times 10^7 M_\odot$ and $\Upsilon_V = 3.72 M_\odot/L_{\odot,V}$, but models with $M_{\text{BH}} = 0$ are consistent at about the 1σ level. The Gauss–Hermite moments of the LOSVD for the best-fit model are shown in Figure 1 and show good agreement with the data. To obtain our final estimates for M_{BH} and Υ_V , we marginalize over the other parameter to get $M_{\text{BH}} = 1.3^{+5.2}_{-1.2} \times 10^7 M_\odot$ and $\Upsilon_V = 3.74 \pm 0.10 M_\odot/L_{\odot,V}$, where the errors are 1σ uncertainties derived from changes from the minimum marginalized χ^2 of $\Delta\chi^2 = 1$. Thus, we cannot rule out the absence of a black hole, but we may put 2σ and 3σ upper limits at $M_{\text{BH}} < 9.6 \times 10^7$ and

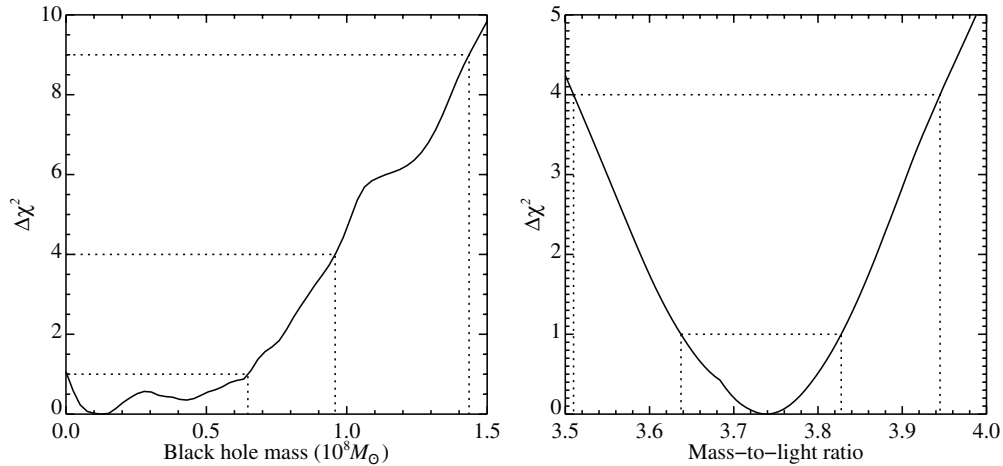


Figure 4. Marginalized $\Delta\chi^2$ curves as a function of M_{BH} (left) and Y_V (right). Dashed lines show intersections of the curves with $\Delta\chi^2 = 1, 4$, and in the case of the top panel, 9, which correspond to the $1\sigma, 2\sigma$, and 3σ confidence levels. There is a slight non-monotonicity in the top panel as one increases in M_{BH} away from the minimum, but it is small and entirely within the 1σ interval. Because the deviations from monotonicity are small (i.e., less than unity), we may be confident that they are not significant. In both cases there is a clear minimum near the best-fit value of each parameter, but in the case of M_{BH} , the data are consistent with $M_{\text{BH}} = 0$ at about the 1σ level.

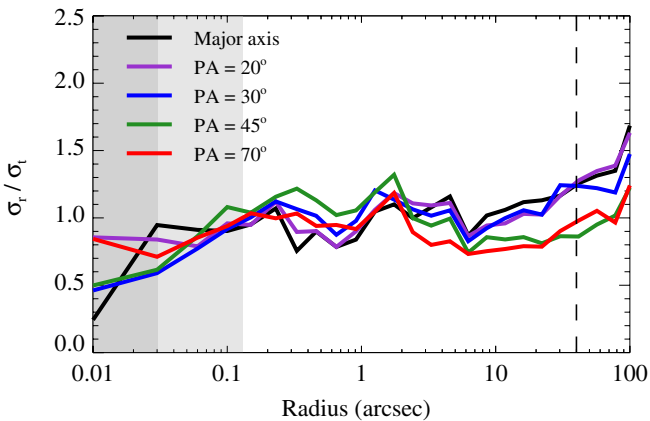


Figure 5. Shape of the velocity dispersion tensor for NGC 4382 from the best-fit model orbit solution. The black line is along the major axis, and the other lines show skew angles with position angles relative to the major axis as given in the legend. The values for the central part of the galaxy are plotted at a radius of $0''.01$. The dashed line shows the radial extent of the ground-based spectroscopic data. The orbits are isotropic until the very center, at which point they become tangentially biased. We indicate the radius of the sphere of influence of a black hole with mass predicted by the $M-\sigma$ relation (light gray) or with our best-fit mass (medium gray).

(A color version of this figure is available in the online journal.)

$M_{\text{BH}} < 1.4 \times 10^8 M_{\odot}$, respectively. We plot marginalize $\Delta\chi^2$ as a function of M_{BH} and Y_V in Figure 4.

Figure 5 shows the velocity dispersion tensor for the best-fit model by plotting the ratio of the radial velocity dispersion (σ_r) to the tangential velocity dispersion (σ_t), defined as $\sigma_r^2 \equiv (\sigma_{\theta}^2 + \sigma_{\phi}^2)/2$, where σ_{ϕ} is the second moment of the azimuthal velocity relative to the systemic velocity rather than relative to the mean rotational speed. An isotropic velocity dispersion would have $\sigma_r/\sigma_t = 1$. Uncertainties are ~ 0.2 , estimated from the smoothness of the profiles (Gebhardt et al. 2003). There is a clear transition at $0''.1$. Outside of this radius, the orbits are roughly isotropic ($\sigma_r/\sigma_t \approx 1$), but inside of this radius the orbits are tangentially biased ($\sigma_r/\sigma_t < 1$). There is a very strong indication of rotation at the center of the model galaxy along the major axis ($\sigma_r/\sigma_t = 0.24$).

4. DISCUSSION

Before discussing the implications of our results, several potential difficulties in interpretation should be mentioned for this galaxy. Our kinematic modeling requires three assumptions: (1) a constant stellar mass-to-light ratio over the range of interest of the galaxy with the exception of the central black hole, (2) axisymmetric mass distribution, and (3) that the system is in dynamical equilibrium. We discuss each of these in turn.

4.1. Constant Y ?

The first of these assumptions, constant mass-to-light ratio, is unlikely to be far from reality. Using *XMM-Newton* and *Chandra* data, Nagino & Matsushita (2009) study the gravitational potential as revealed by X-ray emission from the interstellar medium, assumed to be in hydrostatic equilibrium and spherically symmetric. Within ~ 2 kpc, about the outer extent of our data, they find a constant *B*-band mass-to-light ratio consistent with a potential dominated by stellar mass. Over the range of $0''.2 < r < 10''$ ($\approx 0.2-1$ kpc) NGC 4382 has a shallow $V-I$ color gradient $d(V-I)/d \log(r) = +0.006 \pm 0.003$, i.e., growing bluer with decreasing radius, with $V-I = 1.108 \pm 0.001$ at $r = 1''$ (Lauer et al. 2005). While the sign of the color gradient is unusual, the magnitude is small enough to dismiss worries about changing stellar population in the galaxy.

To quantify the effect of deviations from constant mass-to-light ratio on estimates of black hole mass, we note that when the black hole kinematic influence is barely resolved, M_{BH} and Y are anti-correlated (Gebhardt & Thomas 2009; Schulze & Gebhardt 2011). Thus, if there were unaccounted systematic effects such as a radial gradient in Y , it would increase the uncertainty in M_{BH} . We can easily estimate the magnitude of the effect since it is linear with Y . That is, a 30% change in Y will result in at most a 30% change in M_{BH} inference. Based on the radial color gradient analysis above, the magnitude of any radial Y gradient must be small, a couple of percent at most. Thus, the total systematic uncertainty in M_{BH} is less than a couple of percent.

4.2. Axisymmetric or Eccentric Disk?

The second of these assumptions, axisymmetric mass distribution, is potentially violated. Note that the counter-rotating

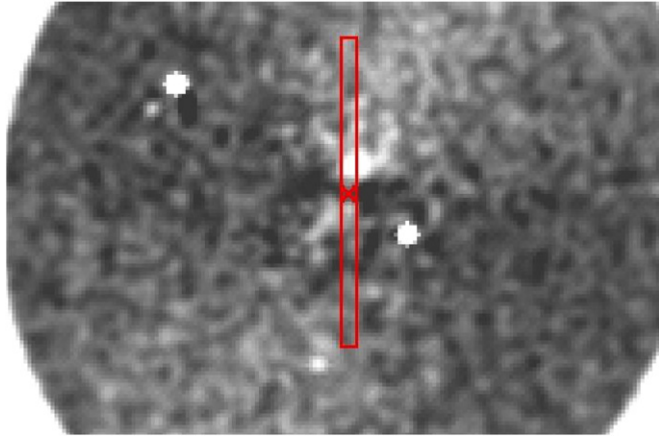


Figure 6. Position of STIS slit from the acquisition camera. This image comes from the STIS acquisition image taken just before the slit and dispersive element were added. We have subtracted a symmetric model for NGC 4382 in order to show the non-symmetric features. The red box shows the location of the slit, and the red cross shows the center position of the galaxy. Up is to the southwest and positive R in Figure 8. The figure shows that the slit does lie on the surface brightness peak.

(A color version of this figure is available in the online journal.)

“kinematically decoupled core” (KDC) found in the OASIS data does not necessarily imply deviations from axisymmetry (McDermid et al. 2004). As can be seen from the images of the galaxy (Figures 6 and 7), the change in ellipticity near the center ($\epsilon = 0.6$ at $r \approx 0''.2$) to the outer regions ($\epsilon = 0.2$ for $r > 1''$) may demonstrate that this system is, overall, triaxial (Chakrabarty 2010). Modeling a truly triaxial system requires a triaxial code (van den Bosch & de Zeeuw 2010), but the case for triaxiality is not straightforward because inside of $0''.2$, the ellipticity decreases again (Lauer et al. 2005).

An alternative interpretation of the two-dimensional photometry is that there are two peaks in surface brightness at the center of the galaxy with projected separation $0''.25$ (Lauer et al. 2005). Such a double nucleus appears to be similar to the double nucleus in M31 (NGC 0224; Lauer et al. 1993), which Tremaine (1995) explained as the result of a projection of a central eccentric disk of stars that is stable only in the presence of a massive dark object, such as a black hole.

This interpretation is born out in the unsymmetrized STIS spectroscopy (Figure 8). There is a prominent increase in the velocity dispersion at the location of the secondary surface brightness peak $R \approx 0''.4$. This would be expected for an eccentric stellar disk.

An eccentric disk cannot be modeled by our orbit superposition code, which forces axisymmetry. In order to estimate the error introduced by forcing axisymmetry, we compared the mass that would be obtained by treating an eccentric disk as though it were a circular orbit. We use the mass estimator $\langle v_x^2 y \rangle$ averaged over the orbit, where v_x is the line-of-sight velocity and y is the distance from the center of light of the orbit on the sky. This is a suitable surrogate for our modeling. We then compare the value of the estimated mass assuming an elliptical orbit to the mass inferred when assuming a circular orbit with the same semi-major axis. Treating an elliptical orbit as though it were a circular orbit produces an error in the black hole mass that depends on the orbit’s eccentricity and orientation. For an eccentricity of 0.60, the error in the black hole mass estimate caused by ignoring the eccentricity varies from -15% to $+7\%$. Orbits with smaller eccentricity produce smaller errors. Given

the statistical uncertainties in our M_{BH} estimate, we can safely ignore this systematic uncertainty.

A consequence of our assumption of axisymmetry is that we are only sensitive to the presence of a black hole at the center of the galaxy. There are two potential issues. The first is whether an existing black hole is located at the center; the second is whether the STIS slit was positioned to allow measurement of any central black hole. We consider both of these.

Because NGC 4382 is a recent merger (see Section 4.3), a relevant question is whether any black hole in the galaxy is located at the center, a requirement for detection with our method. The timescale for a black hole to sink to the center of a galaxy depends on where it starts its descent and in what orbital configuration. In a purely tangential orbit at ~ 20 kpc, it would take longer than a Hubble time to rest at the center, but a radial orbit at ~ 100 pc would take less than ~ 50 Myr. In the most likely case, before the merger, there would be a black hole in the primary galaxy. Following the merger, it is unlikely that it would have traveled farther than ~ 100 pc, and we can expect any such black hole to be at the center now.

Since the center of NGC 4382 is morphologically complex and we have not found strong evidence for a black hole at its center, it is important to determine that the slit was positioned in such a way that the central kinematics could be determined. From the STIS acquisition camera image (Figure 6), it can be clearly ascertained that it does so. This image comes from the STIS acquisition image taken just before the slit and dispersive element were added. We have subtracted a symmetric model for NGC 4382 in order to show the non-symmetric features. The red box shows the location of the slit, and the red cross shows the center position of the galaxy.

4.3. Dynamical Equilibrium?

The third of these assumptions, dynamical equilibrium, is the most important. Our analysis, like any dynamical analysis of this kind, does not handle large deviations from dynamical equilibrium. Schweizer & Seitzer (1992) found a high fine structure index in NGC 4382 of $\Sigma = 6.85$, defined as

$$\Sigma = S + \log(1 + n) + J + B + X, \quad (4)$$

where S is a visual estimate of the strength of the most prominent ripples with range $S = 0-3$, n is the number of detected ripples, J is the number of jets, B is a visual estimate of the maximum boxiness of isophotes, with range $B = 0-3$, and $X = 0$ or 1 indicates the absence or presence of an X -structure, respectively (Schweizer et al. 1990).

Lauer et al. (2005) consider NGC 4382 to be an excellent candidate for a recent merger based on its high value of Σ , one of the three-highest non-merging in the Schweizer & Seitzer (1992) sample, the KDC mentioned above, and the galaxy’s blue average $V - I$ color. Kormendy et al. (2009) note that the strong fine-structure features are also seen in the *gri* Sloan Digital Sky Survey (SDSS) image and interpret this as evidence that the galaxy has recently merged but has not fully relaxed.

The fine structure index, however, is sensitive to gas-rich minor mergers that are unlikely to disturb the entire galaxy or the central parts of the galaxy from an equilibrium condition. Additionally, fine structure may be a poor measure of recent gas-poor major mergers (van Dokkum 2005; Tal et al. 2009). In the case of NGC 4382, the fine structure appears to be “Malin shells,” which can be the result of gas-poor, primarily stellar, mergers (Malin & Carter 1980; Quinn 1984). As a core elliptical

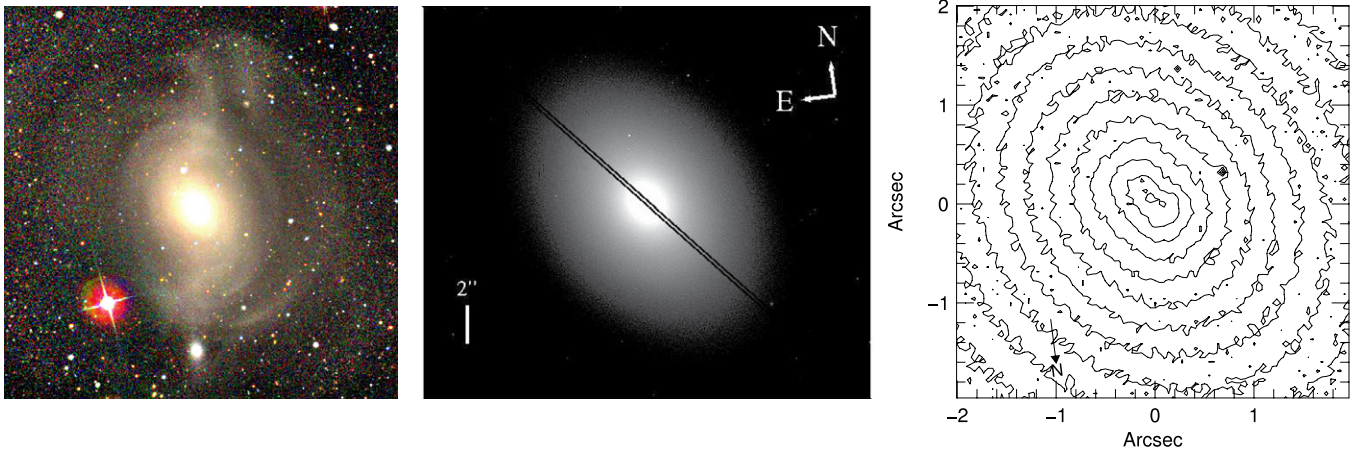


Figure 7. Images of NGC 4382. The left panel shows the Kormendy et al. (2009) wide-field image from SDSS *gri* with a high-pass filter applied to bring out the fine structure, oriented such that north is up and east is left. The center panel is from F555W *HST*/WFPC image and shows the position of the slit with regards to the major axis. The right panel is the Lauer et al. (2005) contour of the same F555W *HST*/WFPC data zoomed in to show the double nucleus. The fine structure and double nucleus are evidence of a possible recent merger in this system. The double nucleus is likely a stellar eccentric nuclear disk in analogy to M31.

(A color version of this figure is available in the online journal.)

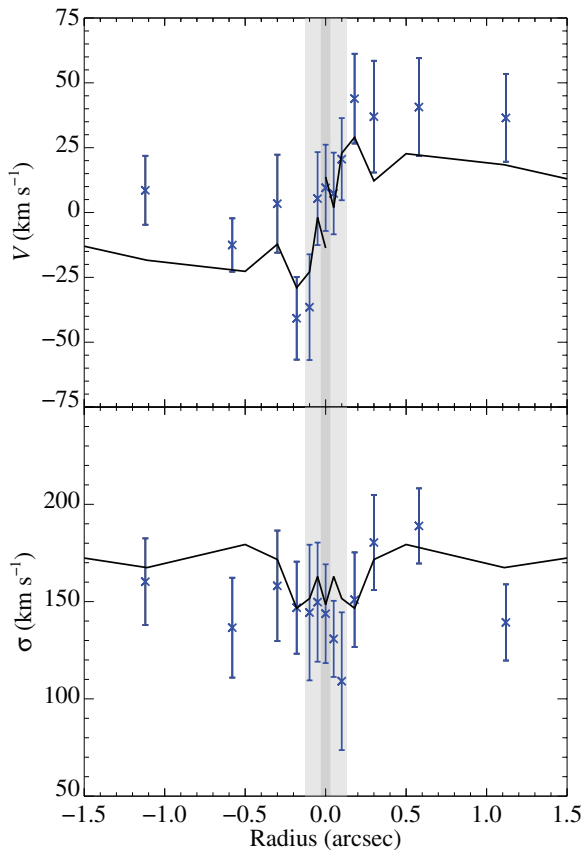


Figure 8. Velocity and velocity dispersion measurements from STIS from both sides of the center. The black line shows the best-fit axisymmetric model. There is a noticeable increase in σ at $R = +0''.5$, which corresponds to the location of the secondary surface brightness peak, indicative of an eccentric stellar disk or torus. We indicate the radius of the sphere of influence of a black hole with mass predicted by the M - σ relation (light gray) or with our best-fit mass (medium gray).

(A color version of this figure is available in the online journal.)

this galaxy is expected to be a mostly gas-poor merger (Lauer et al. 2007b; Kormendy et al. 2009).

The virialization time at the center of the galaxy is much shorter than at the outer regions where the Malin shells are at

apopause and may persist for $\sim 10^8$ yr so that virialization proceeds from the inside out. It is thus not likely to affect the inner portions of the galaxy important for our study (Navarro 1990). As a final comment on the evidence of recent merger activity, we note that Chung et al. (2009) investigated NGC 4382 for signs of interaction motivated by the ~ 35 kpc projected distance from NGC 4395. They found no signatures of interaction in H I or other wavelengths.

So, we urge caution against overinterpretation of our kinematics modeling, but for the remainder of this discussion, we take our results at face value while considering their implications.

4.4. Resolution of the Sphere of Influence

Resolving the sphere of influence of the black hole is desirable but not necessary for measuring the mass (Gültekin et al. 2009c). As the sphere of influence is more and more poorly resolved, the uncertainties in mass increase until the estimate of black hole mass is consistent with zero or even negative (e.g., NGC 3945, Gültekin et al. 2009b). Using our measured effective velocity dispersion of $\sigma_e = 182 \text{ km s}^{-1}$, the black hole mass predicted from the M - σ relation is $M_{\text{BH}} = 8.8 \times 10^7 M_{\odot}$. From Equation (1) the predicted sphere of influence for this object at a distance of 17.9 Mpc has radius $0''.13$ or diameter $0''.26$. The central resolution element of our STIS spectroscopy is $0''.2$ across the slit and $0''.05$ along the slit. Thus, the projection of the predicted sphere of influence fits entirely inside of the central resolution element. Based on our best-fit mass estimate of $M_{\text{BH}} = 1.3 \times 10^7 M_{\odot}$, the radius of the sphere of influence is $0''.03$ (diameter $0''.06$), where the velocity dispersion is 145 km s^{-1} . The diameter of the actual sphere of influence is thus about the size of the pixel but 3.3 times smaller than the slit width. At such low resolution, it is typical to find an upper limit to the mass of the black hole, as we have here. The 1σ upper bound to the black hole mass is $M_{\text{BH}} = 6.5 \times 10^7 M_{\odot}$, which has a sphere of influence radius $0''.13$, the same as the predicted sphere of influence.

4.5. Is the Black Hole Mass Anomalously Low?

Our modeling reveals that the kinematic observations are consistent with no black hole in NGC 4382 at about the 1σ level. If there were, in fact, no black hole in NGC 4382, it would be

one of only two early-type galaxies with upper limits on their black hole mass below that predicted by the scaling relations. The other is NGC 3945, but the double bars in that galaxy may prevent reliable black hole mass estimation (Gültekin et al. 2009b). Given that our mass measurement does not completely rule out the presence of a black hole, we consider whether NGC 4382 is a unique object or merely lies along the low-end tail of the distribution of black hole masses for a given host galaxy property.

Based on the M – σ relation ($M_{\text{BH}}/M_{\odot} = 10^{8.12} (\sigma_e/200 \text{ km s}^{-1})^{4.24}$; Gültekin et al. 2009c), the mean logarithmic black hole mass for a galaxy with $\sigma = 182 \text{ km s}^{-1}$ is $\log(M_{\text{BH}}/M_{\odot}) = 7.95$, corresponding to $M_{\text{BH}} = 8.8 \times 10^7 M_{\odot}$. The scatter in the M – σ relation is lognormal with standard deviation $\epsilon_0 = 0.31 \pm 0.06$ for the population of ellipticals. Taking the scatter into account, the 68% confidence interval of black hole mass is $M_{\text{BH}} = 4.0 \times 10^7$ to $1.8 \times 10^8 M_{\odot}$, which is consistent within our 1σ mass estimate.

To calculate the mass expected from the M – L relation ($M_{\text{BH}}/M_{\odot} = 10^{8.95} (L_V/10^{11} L_{\odot,V})^{1.11}$; Gültekin et al. 2009c), we must first find the luminosity of the bulge. The total luminosity of the galaxy may be obtained from $M_V = -22.54 \pm 0.05$ (Kormendy et al. 2009) using $\log(L_V/L_{\odot,V}) = 0.4(4.83 - M_V)$ (cf. Verbunt 2008). Given that we are adopting the more modern classification of E2, this galaxy is “all bulge,” and so the luminosity is $L_V = 8.9 \times 10^{10} L_{\odot,V}$. The mean logarithmic mass for such a galaxy is $\log(M_{\text{BH}}/M_{\odot}) = 8.89$ or $M_{\text{BH}} = 7.8 \times 10^8 M_{\odot}$. Taking the $\epsilon_0 = 0.38 \pm 0.09$ scatter in the relation into account, the 68% confidence interval in mass is $M_{\text{BH}} = 3.0 \times 10^8$ to $2.1 \times 10^9 M_{\odot}$. The lower limit of this range is more than a factor of 2 larger than our 3σ upper limit for the black hole mass. In this sense, the black hole mass is anomalously low.

In order to be consistent with the M – σ relation but low according to the M – L relation, NGC 4382 cannot lie on the mean Faber & Jackson (1976) L – σ relation. In fact, core galaxies with $M_V = -22.54$ have a mean logarithmic velocity dispersion corresponding to $\sigma = 253 \text{ km s}^{-1}$, compared to our measured value of $\sigma_e = 182 \text{ km s}^{-1}$.

The stellar mass of the bulge is $M_* = L_V \Upsilon_V = 3.3 \times 10^{11} M_{\odot}$. This is consistent with g - and z -band model magnitudes, which give $M_* = 4.0 \times 10^{11} M_{\odot}$ (Bell et al. 2003; Gallo et al. 2010). Thus, $M_{\text{BH}}/M_* = 3.9 \times 10^{-5}$ compared to the standard 1.3×10^{-3} value (Kormendy & Gebhardt 2001). Using the 3σ upper mass bound, the ratio is $M_{\text{BH}}/M_* = 4.2 \times 10^{-4}$, still a factor of 3 lower. In Section 4.6, we discuss how our value of Υ_V may be wrong because we do not include a dark matter halo in our modeling, but this is only likely to result in a small (5%–10%) decrease in Υ_V (Gebhardt & Thomas 2009; Schulze & Gebhardt 2010).

Like many other early-type galaxies, NGC 4382 has a flat luminosity core. It has been argued that the cores are scoured out by the inspiral of black holes during galaxy mergers (Begelman et al. 1980; Ebisuzaki & Makino 1995; Faber et al. 1997; Volonteri et al. 2003a, 2003b; Milosavljević & Merritt 2003; Lauer et al. 2007b; Kormendy & Bender 2009). This process ejects stars on elongated orbits and leads to tangentially biased stellar distribution functions (See Figure 5). The galaxy’s core can be described by its stellar mass “deficit,” the mass in stars ejected from what was previously a power-law profile. The most recent numerical simulations on black hole mergers find that for nearly equal masses, the mass deficit should scale with the total mass of the binary (Merritt 2006), but for mass ratios far

from unity, the mass deficit should scale with the mass of the secondary (Sesana et al. 2008).

Kormendy & Bender (2009) included NGC 4382 in their study of the correlations between black hole mass and mass deficits. They estimated $M_{\text{BH}} = 1.0 \times 10^8 M_{\odot}$ by assuming that it follows the Tremaine et al. (2002) M – σ relation, and they estimated $\Upsilon_V = 8.3$ by assuming that it follows $\Upsilon_V \propto L_V^{0.36}$ due to Cappellari et al. (2006). Using the photometry from Kormendy et al. (2009), they measured a luminosity deficit of $1.6 \times 10^8 L_{\odot,V}$. For their assumed values of M_{BH} and Υ_V , NGC 4382 lies along the same correlation between M_{BH} and mass deficit as the rest of their sample (roughly $M_{\text{deficit}} = 10 M_{\text{BH}}$). Using the values for M_{BH} and Υ_V we measure here, NGC 4382 appears to have a small black hole mass for its core mass deficit, but is consistent at the 1σ level. For our best estimate of the mass, $M_{\text{deficit}}/M_{\text{BH}} = 45.6$, and for the 1σ upper bound of the mass, $M_{\text{deficit}}/M_{\text{BH}} = 9.1$. Kormendy & Bender (2009) also found that the ratio of light deficit to total bulge luminosity ($L_{V,\text{deficit}}/L_V = 1.8 \times 10^{-3}$ for NGC 4382) scales with the ratio of black hole mass to bulge stellar mass. Using their empirical correlation and our measured value of M_{BH}/M_* predicts a ratio of $L_{V,\text{deficit}}/L_V = 2.0 \times 10^{-4}$. With our 1σ upper bound on M_{BH} , it predicts $L_{V,\text{deficit}}/L_V = 1.7 \times 10^{-3}$, consistent with the observed value within the total scatter of the relation. So, it appears that, in sum, the mass of any black hole in NGC 4382 is consistent with M – σ and core scaling properties but low based on M – L .

The low black hole mass does, however, clear up an apparent disparity in nuclear activity. The nuclear X-ray luminosity between 0.3 and 10 keV is less than $L_X < 2.7 \times 10^{38} \text{ erg s}^{-1}$ (Sivakoff et al. 2003; Gallo et al. 2010). The core was also not detected in radio, typically considered a proxy for jet activity from an accreting black hole. With an X-ray limit and a radio detection, a black hole mass limit can be estimated (Gültekin et al. 2009a). Very Large Array observations at 8.4 GHz, however, did not detect any core radio emission with a 3σ upper limit of $F_{\text{core}} < 0.11 \text{ mJy}$ (Capetti et al. 2009). Capetti et al. (2009) note that it is concerning that a galaxy as large as NGC 4382 shows no sign of nuclear activity. Their argument is that, under the assumption that NGC 4382 hosts a $M_{\text{BH}} \sim 10^8 M_{\odot}$ supermassive black hole as would be expected from galaxy properties, the absence of nuclear activity in X-ray and radio bands indicates a failure of AGN activity to trace black holes. Even a small amount of ambient gas could produce enough radio emission to be visible for a large black hole. Our black hole mass estimate, however, indicates that it is more likely that NGC 4382 either has no black hole or a black hole that is far undermassive for its host galaxy properties. Therefore, the lack of any nuclear activity accurately traces the small or non-existent black hole in line with predictions for and existing observations of the AGN fraction in Virgo cluster galaxies (Volonteri et al. 2008; Gallo et al. 2008).

4.6. Mass-to-light Ratio

Although this work does not unambiguously detect a black hole, the mass-to-light ratio was determined precisely, $\Upsilon_V = 3.74 \pm 0.10 M_{\odot}/L_{\odot,V}$, owing to the good coverage and high quality of the SAURON data. Unfortunately, NGC 4382 was not one of the galaxies modeled by Cappellari et al. (2006) so no direct comparison can be made. Note that we do not explicitly include a dark matter halo in our modeling. This is unlikely to affect our black hole mass results on account of the high spatial resolution provided by *HST*/STIS (Gebhardt et al. 2011). The

stellar mass-to-light ratio, however, is likely to be affected by not including this component. While the inferred stellar mass-to-light ratio changed by a factor of 2 when including or omitting a dark matter component in the modeling for M87 (Gebhardt & Thomas 2009), the high spatial resolution in our data sets is likely to result in only a small (5%–10%) decrease in Y_V (Schulze & Gebhardt 2010). Galaxies with $M_V = -22.54$ have a mean mass-to-light ratio $Y_V = 6.7$ (Lauer et al. 2007a). Based on the scaling relation between Y_I and stellar velocity dispersion in ellipticals (Cappellari et al. 2006), the implied typical value for a galaxy with $\sigma_e = 182 \text{ km s}^{-1}$ is roughly $Y_V \approx 5.3$. The low value of Y_V in NGC 4382 compared to established ellipticals suggests ongoing star formation and would be expected for a recent merger.

We thank Scott Tremaine for helpful discussions about this work and the SAURON team for making their data available to the community. We thank the anonymous referee for useful comments. The modeling made use of the facilities at the Texas Advanced Computing Center at the University of Texas at Austin. This work made use of the NASA's Astrophysics Data System (ADS), and the NASA/IPAC Extragalactic Database (NED), which is operated by the Jet Propulsion Laboratory, California Institute of Technology, under contract with the National Aeronautics and Space Administration. This research has made use of the VizieR catalogue access tool, CDS, Strasbourg, France. Financial support was provided by NASA/HST grants GO-7468, and GO-9107 from the Space Telescope Science Institute, which is operated by AURA, Inc., under NASA contract NAS 5-26555. K.Gü. acknowledges support provided by the National Aeronautics and Space Administration through Chandra Award Number GO0-11151X issued by the Chandra X-ray Observatory Center, which is operated by the Smithsonian Astrophysical Observatory for and on behalf of the National Aeronautics Space Administration under contract NAS8-03060. D.O.R. thanks the Institute for Advanced Study and acknowledges support of a Corning Glass Works Foundation Fellowship. K.Ge. acknowledges support from NSF-0908639.

REFERENCES

- Aller, M. C., & Richstone, D. O. 2007, *ApJ*, **665**, 120
 Bacon, R., Copin, Y., Monnet, G., et al. 2001, *MNRAS*, **326**, 23
 Begelman, M. C., Blandford, R. D., & Rees, M. J. 1980, *Nature*, **287**, 307
 Bell, E. F., McIntosh, D. H., Katz, N., & Weinberg, M. D. 2003, *ApJS*, **149**, 289
 Bentz, M. C., Peterson, B. M., Pogge, R. W., Vestergaard, M., & Onken, C. A. 2006, *ApJ*, **644**, 133
 Bower, R. G., Benson, A. J., Malbon, R., et al. 2006, *MNRAS*, **370**, 645
 Burkert, A., & Tremaine, S. 2010, *ApJ*, **720**, 516
 Capetti, A., Kharb, P., Axon, D. J., Merritt, D., & Baldi, R. D. 2009, *AJ*, **138**, 1990
 Cappellari, M., Bacon, R., Bureau, M., et al. 2006, *MNRAS*, **366**, 1126
 Chakrabarty, D. 2010, *A&A*, **510**, A45
 Chung, A., van Gorkom, J. H., Kenney, J. D. P., Crowl, H., & Vollmer, B. 2009, *AJ*, **138**, 1741
 de Vaucouleurs, G., de Vaucouleurs, A., Corwin, H. G., et al. 1991, Third Reference Catalogue of Bright Galaxies (Berlin: Springer)
 de Zeeuw, P. T., Bureau, M., Emsellem, E., et al. 2002, *MNRAS*, **329**, 513
 Dressler, A. 1989, in IAU Symp. 134, Active Galactic Nuclei, ed. D. E. Osterbrock & J. S. Miller (Dordrecht: Kluwer), 217
 Ebisuzaki, T., & Makino, J. 1995, *Astron. Her.*, **88**, 238
 Emsellem, E., Cappellari, M., Peletier, R. F., et al. 2004, *MNRAS*, **352**, 721
 Faber, S. M., & Jackson, R. E. 1976, *ApJ*, **204**, 668
 Faber, S. M., Tremaine, S., Ajhar, E. A., et al. 1997, *AJ*, **114**, 1771
 Ferrarese, L., Côté, P., Dalla Bontà, E., et al. 2006, *ApJ*, **644**, L21
 Ferrarese, L., & Merritt, D. 2000, *ApJ*, **539**, L9
 Fisher, D. 1997, *AJ*, **113**, 950
 Gallo, E., Treu, T., Jacob, J., et al. 2008, *ApJ*, **680**, 154
 Gallo, E., Treu, T., Marshall, P. J., et al. 2010, *ApJ*, **714**, 25
 Gebhardt, K., Adams, J., Richstone, D. O., et al. 2011, *ApJ*, **729**, 119
 Gebhardt, K., Bender, R., Bower, G., et al. 2000, *ApJ*, **539**, L13
 Gebhardt, K., Richstone, D., Tremaine, S., et al. 2003, *ApJ*, **583**, 92
 Gebhardt, K., & Thomas, J. 2009, *ApJ*, **700**, 1690
 Graham, A. W. 2004, *ApJ*, **613**, L33
 Greene, J. E., Peng, C. Y., Kim, M., et al. 2010, *ApJ*, **721**, 26
 Gültekin, K., Cackett, E. M., Miller, J. M., et al. 2009a, *ApJ*, **706**, 404
 Gültekin, K., Richstone, D. O., Gebhardt, K., et al. 2009b, *ApJ*, **695**, 1577
 Gültekin, K., Richstone, D. O., Gebhardt, K., et al. 2009c, *ApJ*, **698**, 198
 Häring, N., & Rix, H.-W. 2004, *ApJ*, **604**, L89
 Hopkins, P. F., Hernquist, L., Cox, T. J., Robertson, B., & Krause, E. 2007, *ApJ*, **669**, 67
 Hopkins, P. F., Hernquist, L., Cox, T. J., et al. 2006, *ApJS*, **163**, 1
 Hu, J. 2008, *MNRAS*, **386**, 2242
 Kormendy, J. 1993, in The Nearest Active Galaxies, ed. J. Beckman, L. Colina, & H. Netzer (Madrid: Consejo Superior de Investigaciones Científicas), 197
 Kormendy, J., & Bender, R. 2009, *ApJ*, **691**, L142
 Kormendy, J., Bender, R., & Cornell, M. E. 2010, *Nature*, **469**, 374
 Kormendy, J., Fisher, D. B., Cornell, M. E., & Bender, R. 2009, *ApJS*, **182**, 216
 Kormendy, J., & Gebhardt, K. 2001, in AIP Conf. Ser. 586, Relativistic Astrophysics, ed. J. C. Wheeler & H. Martel (Melville, NY: AIP), 363
 Kormendy, J., & Richstone, D. 1995, *ARA&A*, **33**, 581
 Krajnović, D., McDermid, R. M., Cappellari, M., & Davies, R. L. 2009, *MNRAS*, **399**, 1839
 Kuo, C. Y., Braatz, J. A., Condon, J. J., et al. 2010, *ApJ*, **727**, 20
 Laor, A. 2001, *ApJ*, **553**, 677
 Lauer, T. R., Ajhar, E. A., Byun, Y.-I., et al. 1995, *AJ*, **110**, 2622
 Lauer, T. R., Faber, S. M., Gebhardt, K., et al. 2005, *AJ*, **129**, 2138
 Lauer, T. R., Faber, S. M., Groth, E. J., et al. 1993, *AJ*, **106**, 1436
 Lauer, T. R., Faber, S. M., Richstone, D., et al. 2007a, *ApJ*, **662**, 808
 Lauer, T. R., Gebhardt, K., Faber, S. M., et al. 2007b, *ApJ*, **664**, 226
 Magorrian, J., Tremaine, S., Richstone, D., et al. 1998, *AJ*, **115**, 2285
 Malin, D. F., & Carter, D. 1980, *Nature*, **285**, 643
 Marconi, A., & Hunt, L. K. 2003, *ApJ*, **589**, L21
 McDermid, R., Emsellem, E., Cappellari, M., et al. 2004, *Astron. Nachr.*, **325**, 100
 McLure, R. J., & Dunlop, J. S. 2002, *MNRAS*, **331**, 795
 Merritt, D. 2006, *ApJ*, **648**, 976
 Michard, R., & Marchal, J. 1994, *A&AS*, **105**, 481
 Milosavljević, M., & Merritt, D. 2003, *ApJ*, **596**, 860
 Milosavljević, M., Merritt, D., Rest, A., & van den Bosch, F. C. 2002, *MNRAS*, **331**, L51
 Nagino, R., & Matsushita, K. 2009, *A&A*, **501**, 157
 Navarro, J. F. 1990, *MNRAS*, **242**, 311
 Nowak, N., Thomas, J., Erwin, P., et al. 2010, *MNRAS*, **403**, 646
 Onken, C. A., Ferrarese, L., Merritt, D., et al. 2004, *ApJ*, **615**, 645
 Paturel, G., Petit, C., Prugniel, P., et al. 2003, *A&A*, **412**, 45
 Pence, W. 1998, in ASP Conf. Ser. 145, Astronomical Data Analysis Software and Systems VII, ed. R. Albrecht, R. N. Hook, & H. A. Bushouse (San Francisco, CA: ASP), 97
 Pinkney, J., Gebhardt, K., Bender, R., et al. 2003, *ApJ*, **596**, 903
 Quinn, P. J. 1984, *ApJ*, **279**, 596
 Ravindranath, S., Ho, L. C., & Filippenko, A. V. 2002, *ApJ*, **566**, 801
 Rees, M. J. 1984, *ARA&A*, **22**, 471
 Richstone, D., Ajhar, E. A., Bender, R., et al. 1998, *Nature*, **395**, A14
 Schulze, A., & Gebhardt, K. 2010, *ApJ*, **729**, 21
 Schulze, A., & Gebhardt, K. 2011, *ApJ*, **729**, 21
 Schweizer, F., & Seitzer, P. 1992, *AJ*, **104**, 1039
 Schweizer, F., Seitzer, P., Faber, S. M., et al. 1990, *ApJ*, **364**, L33
 Sesana, A., Haardt, F., & Madau, P. 2008, *ApJ*, **686**, 432
 Siopis, C., Gebhardt, K., Lauer, T. R., et al. 2009, *ApJ*, **693**, 946
 Sivakoff, G. R., Sarazin, C. L., & Irwin, J. A. 2003, *ApJ*, **599**, 218
 Tal, T., van Dokkum, P. G., Nelan, J., & Bezanson, R. 2009, *AJ*, **138**, 1417
 Tremaine, S. 1995, *AJ*, **110**, 628
 Tremaine, S., Gebhardt, K., Bender, R., et al. 2002, *ApJ*, **574**, 740
 van den Bosch, R. C. E., & de Zeeuw, P. T. 2010, *MNRAS*, **401**, 1770
 van Dokkum, P. G. 2005, *AJ*, **130**, 2647
 Verbunt, F. 2008, arXiv:0807.1393
 Volonteri, M. 2007, *ApJ*, **663**, L5
 Volonteri, M., Haardt, F., & Gültekin, K. 2008, *MNRAS*, **384**, 1387
 Volonteri, M., Haardt, F., & Madau, P. 2003a, *ApJ*, **582**, 559
 Volonteri, M., Madau, P., & Haardt, F. 2003b, *ApJ*, **593**, 661
 Woo, J.-H., Treu, T., Barth, A. J., et al. 2010, *ApJ*, **716**, 269